Nano Res
DOI 10.1007/s12274-012-0251-0
Research Article

ISSN 1998-0124
CN 11-5974/O4

Terahertz Graphene Optics

Nima Rouhi[1], Santiago Capdevila[2], Dheeraj Jain[1], Katayoun Zand[1], Yung Yu Wang[1], Elliott Brown[3], Lluis Jofre[2], and Peter Burke[1] (✉)

[1] Integrated Nanosystems Research Facility, Department of Electrical Engineering and Computer Science, University of California, Irvine, CA 92697, USA
[2] Universitat Politècnica de Catalunya, Barcelona, Spain
[3] Wright State University, Dayton, OH 45435, USA

Received: 13 June 2012 / Revised: 7 August 2012 / Accepted: 9 August 2012

ABSTRACT

The magnitude of the optical sheet conductance of single-layer graphene is universal, and equal to $e^2/4\hbar$ (where $2\pi\hbar = h$ (the Planck constant)). As the optical frequency decreases, the conductivity decreases. However, at some frequency in the THz range, the conductivity increases again, eventually reaching the DC value, where the magnitude of the DC sheet conductance generally displays a sample- and doping-dependent value between ~e^2/h and 100 e^2/h. Thus, the THz range is predicted to be a non-trivial region of the spectrum for electron transport in graphene, and may have interesting technological applications. In this paper, we present the first frequency domain measurements of the absolute value of multilayer graphene (MLG) and single-layer graphene (SLG) sheet conductivity and transparency from DC to 1 THz, and establish a firm foundation for future THz applications of graphene.

KEYWORDS

Single-layer graphene, terahertz, conductance, multilayer graphene, broadband

1. Introduction

Two of the most fundamental and defining properties of graphene are (1) the universal conductivity ($e^2/4\hbar$) [1] at optical frequencies, and (2) the high sheet carrier density and mobility at DC (giving increased conductivities up to 100 times larger than the optical conductivities). However, in the spectral region in between the transition has not yet been mapped out. Starting from the optical and going down, as the frequency is lowered below the Fermi energy (over h), electron–hole pair generation (inter-band) absorption ceases, and the system becomes insulating (i.e. the conductivity goes to zero). As the frequency is lowered even further, the conductivity eventually rises again, approaching the DC value of up to 100 times its optical value. However, to date this transition has not been mapped out experimentally down to the technologically-important radiofrequency (RF) region ($\leqslant$1 THz).

Several groups have studied single-layer graphene using Fourier transform infrared spectroscopy (FTIR) techniques to map the transition from the visible down, demonstrating the drop in the optical conductivity as the frequency drops below the Fermi energy [2]. As the frequency goes lower, even the very first measurements of this effect [2] observed

Address correspondence to pburke@uci.edu

a slight rise in the conductivity, measured down to 20 THz, attributed to the intraband or "Drude" scattering. Subsequent experiments from many groups have observed this using FTIR down to 1 THz [3–5], and inferred a Drude scattering time of 300 fs ($1/\Gamma$) for samples with mobility of ~1000–3000 $cm^2/(V \cdot s)$. With this value of the scattering time, the graphene sheet conductivity is predicted to vary by a factor of almost an order of magnitude between DC and 1 THz, but because of the difficulty in scaling down FTIR techniques below 1 THz, this was not measurable. In addition, most of the far-IR work to date has only measured the relative change in transparency/reflectivity/conductivity, and not the absolute value, which is more difficult to ascertain. A complementary time-domain (sub-ps pulse) technique has demonstrated sheet conductivity of single-layer graphene of up to 30 $e^2/4\hbar$ from 0.5–2 THz at room temperature [6], and low temperatures [7]. These time-domain techniques provide lower spectral resolution than the continuous wave (CW) frequency-domain techniques presented here, but in principle yield the same physical information.

Researchers have also investigated the sheet conductance of multilayer graphene (MLG) as a function of frequency. Although different in principle, interactions between the layers (at visible and IR frequencies) have been shown to have only minimal impact on the overall sheet conductance, which behaves essentially as N times that of an individual layer (N = number of layers) [8]. However, subsequent detailed studies have shown some resonance behavior in the IR sheet conductivity due to interlayer interactions [9]. The THz-to-IR frequency dependence of few and multilayer graphene on SiC was shown to have the predicted Drude behavior down to 1.5 THz with a scattering time of 40 fs [10], and down to 600 GHz with a scattering time of 10 fs and sheet conductance up to 20 $e^2/4\hbar$ [11]. Kim and co-workers at Sungkyunkwan University (SKKU) in Korea used FTIR down to 1 THz [12] where a Drude scattering time of ~300 fs was found, surprisingly independent of the DC mobility, which varied by over an order of magnitude (from 1000 to 10000 $cm^2/(V \cdot s)$).

Coming up from DC, some groups have used microwave (waveguide) techniques. A 13 GHz dielectric resonance oscillator (DRO) measurement (spot frequency) of multilayer graphene on SiC was made by Krupka, but the per layer conductance was not determined [13, 14]. An on-chip coplanar waveguide measurement technique was recently employed to study single-layer graphene (SLG) up to 110 GHz [15]. Scanned probe microwave microscopy of single and multilayer graphene has been used to image electrical properties at GHz frequencies, although determination of the absolute sheet conductivity is difficult with this technique [16, 17].

While the determination of the real conductivity is significant, its interaction with the imaginary part and applications in plasmonics may be even more interesting. Rana proposed a THz plasmon laser [18]. The Drude frequency dependence of the two-dimensional (2D) conductance is equivalent to a plasmon excitation description, as one of us showed previously [19]. Recently, the fundamental resonance of plasmon excitations was observed [4] in graphene ribbons, which is completely analogous to 2D plasmons observed in low mobility 2D electron gases (2DEGs) by Tsui, Allen et al. in the 1970s [20] and by one of us in high mobility 2DEGs in the 2000s [19, 21]. These concepts may lead to tunable graphene based antennas [22] or even nano-antennas [23–28]. At the same time, the detailed theory of the frequency-dependent conductance of graphene, especially in the THz range, is still under development [29, 30]. The theory is somewhat more complex, due to the linear Dirac dispersion curve, the impact of many-body effects on the dynamical properties, and the confluence of the temperature, Fermi energy, and lifetime (all as comparable energies) in the THz to mid IR range.

Thus, to date there has been no comprehensive study from microwave to THz of the broadband conductivity in the frequency domain of either single or multilayer graphene. In this work, we present the first measurements of the absolute value of multilayer and single-layer sheet conductivity and transparency from DC to 1 THz. We use three different, complementary techniques (wave-guide, quasi-optical, and optical) to acquire data over two decades in frequency from 10 GHz to 1000 GHz, and demonstrate the first-ever absolute measurements of the conductivity of both single and multilayer graphene in

this technologically important frequency range. A unique aspect of our work is the application of a continuously tunable THz frequency domain spectrometer. Taken collectively, this work establishes a firm foundation for future THz applications of graphene.

2. Experimental

2.1 Sample preparation and characterization

Because of the techniques used for RF characterization, we require large area graphene sheets and thus, chemical vapor deposition (CVD) grown graphene was transferred onto insulating (quartz, single crystal) substrates according to published recipes [31] (details are provided in the Electronic Supplementary Material (ESM)). Briefly, CVD graphene grown on nickel yielded few-layer graphene, and low pressure CVD (LPCVD) graphene grown on copper yielded nominally single-layer graphene as opposed to atmospheric pressure CVD (AP-CVD) grown graphene on copper which is known to have significant turbostratic graphene and multilayer areas [32]. These statements are justified in the ESM where characterization by optical imaging, Raman spectrum analysis, and atomic force microscopy (AFM) was used to precisely determine the number of layers in our samples especially for single-layer graphene (Figs. S-1–S-3 in the Electronic Supplementary Material (ESM)). The as-grown graphene on metal was coated with PMMA (polymethyl methacrylate), and transferred to single-crystal quartz [33]. All of our samples were found to be quite uniform, consisting of an average of 3–4 layers for the Ni-grown graphene (MLG), and nominally a single-layer for the LPCVD Cu-grown graphene. Several samples of each type were measured (see the ESM for details), but only representative data are presented here (Fig. 1).

2.2 Dynamical impedance techniques

Several techniques exist for material characterization at microwave frequencies of which the most relevant are resonant-cavity and transmission-line techniques [34, 35]. Resonant techniques give the most accurate measurements but are usually limited to a single frequency. These techniques rely on the perturbation of a cavity when the sample is introduced in the region of strong field. The variation in the frequency and the Q-factor of the cavity are then related to the permittivity and conductivity of the sample. This technique has been used previously [13] for the measurement of the sheet resistance of epitaxial graphene at 12 GHz.

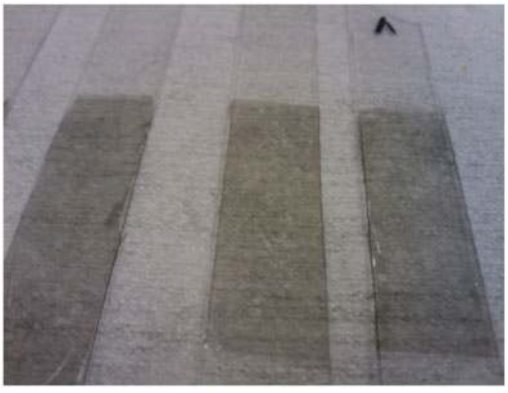

Figure 1 Close-up view of samples MLG#5, MLG#6, and MLG#7 of multilayer graphene already transferred onto quartz substrates

On the other hand, transmission-line techniques extract the material parameters from the strength of the transmitted wave through the sample. Since it does not rely on the excitation of a specific resonant mode, this technique is inherently broadband, limited only by the dimensions of the sample and its homogeneity, to avoid diffraction and scattering effects. In this paper, we use transmission-line techniques for the measurement of the conductivity of several samples of graphene for a broad range of frequencies including X-band (7–13 GHz), W-band (75–110 GHz) and wideband (0.1–1.0 THz).

2.3 Transmission formulation

The measured samples consisted of a SLG or MLG film on top of a substrate of single-crystal quartz. The SLG and MLG films had lateral dimensions of 14 mm × 25 mm and 10 mm × 25 mm, respectively. The lateral dimensions are large enough to utilize RF propagation perpendicular to the film, as displayed in Fig. 2, and to model each graphene-on-quartz sample as a stratified medium.

Usually propagation is then analyzed through two coupled dielectric etalons of different thickness and electrical properties, taking into account the angles of incidence transmission coefficient, and propagation

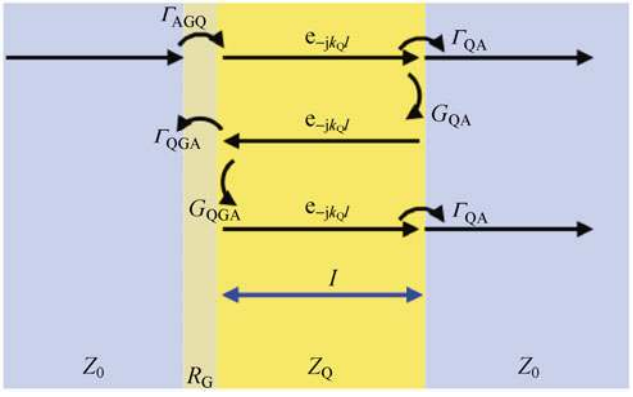

Figure 2 The samples can be considered as stratified media composed of graphene and quartz and surrounded by air

constant, as well as the multiple reflections and refractions in each dielectric [36]. Here, we consider only perpendicular propagation and because the graphene is so much thinner than an RF wavelength, we treat it simply as a lumped impedance [37]. Therefore the model becomes a substrate of quartz surrounded by air on one side and a shunt impedance Z_G representing the graphene film on the other side (see the ESM for an alternative paragraph for RF transmissivity in terms of transmission-line + equivalent-circuit modeling). In this case the transmission coefficient (τ_{AGQ}) from air into the quartz through the graphene sheet is

$$\tau_{AGQ} = 2\left(1+\frac{Z_0}{Z_Q}+\frac{Z_0}{R_G}\right) \quad (1)$$

where Z_0 and Z_Q are the wave impedance in air and the quartz substrate, respectively. After the wave has entered into the quartz substrate part of it is transmitted through the opposite interface (τ_{QA}) and part of it is reflected (Γ_{QGA}, Γ_{QA}). Depending on the thickness of the substrate and the bandwidth of the measurement, the delay between reflections might be large enough that each transmitted reflection can be isolated from the previous (THz time domain measurement) or they might overlap in time leading to a more complex expression that combines all subsequent internal reflection. For the former, it can be shown that the transmitted coefficient for the first pulse becomes

$$S_{21}^{THz} = \tau_{AGQ}\tau_{QA}e^{-jk_Q l} = \frac{4e^{-jk_Q l}}{\frac{(Z_0+Z_Q)^2}{Z_Q+Z_0}+\frac{(Z_0+Z_Q)}{R_G}} \quad (2)$$

where k_Q is the wavenumber in the substrate, and l its thickness. For the latter the transmitted coefficient is [37]

$$S_{21} = \frac{\tau_{AGQ}\tau_{QA}e^{-jk_Q l}}{1-\Gamma_{QGA}\Gamma_{QA}e^{-jk_Q l}} = \frac{2}{\left(2+\frac{Z_0}{R_G}\right)\cos(k_Q l)+j\left(\frac{Z_0}{Z_Q}+\frac{Z_Q}{Z_0}+\frac{Z_Q}{R_G}\right)\sin(k_Q l)} \quad (3)$$

Equation (3) can be also obtained by analyzing the propagation in the equivalent circuit model of Fig. 3, where each layer is represented by a transmission line of characteristic impedance equal to the wave impedance, and the boundary condition is that the graphene layer becomes a parallel resistance R_G.

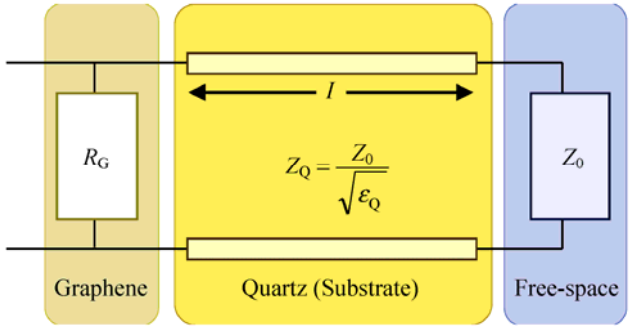

Figure 3 Transmission-line model of a quartz substrate with a graphene sheet on an incident interface

3. X-band measurements

For the X-band measurement the sample dimensions are not large enough for a free-space measurement; instead they are only suitable for waveguide-coupled experiment, as shown in Fig. 4. To guarantee that only the fundamental mode (TE_{10}) is excited in the waveguide, the frequency band is limited from 7 to 13 GHz. Additionally to accommodate the single-layer sample, which is slightly wider (14 mm) than a nominal X-band waveguide WR-90 (10.2 mm), a tapered waveguide transition was machined. The smooth transition prevents the excitation of higher-order modes in the waveguide.

To maximize the attenuation effect of graphene on the transmitted signal, the sample must be oriented so that the electric field excites currents in it, therefore

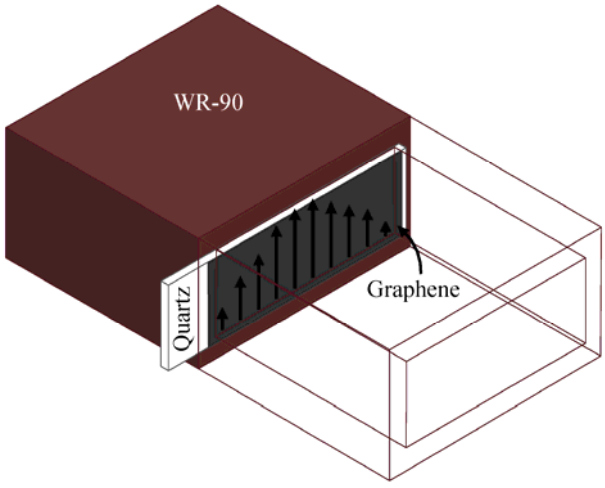

Figure 4 Experimental setup for the X-band measurement, where the wave has a normal incidence with respect to the graphene layer

the surface must be parallel to the polarization of the electric field (vertical for the TE_{10} mode). Our technique maximizes this effect by orienting graphene sheet perpendicular to the waveguide, as shown in Fig. 4. With a perpendicular configuration the sample does not need to be larger than the section of the waveguide, and the power loss is analyzed with the formulation previously introduced.

The measurement uses two coaxial-to-WR-90 waveguide transitions connected to a network analyzer, and the effect of the transitions is removed by using a TRL (thru-reflect-line) calibration (see the ESM). Figure 5 presents the attenuation (measured S_{21}) introduced by a reference bare quartz substrate as well as one of the single-layer and multilayer graphene samples (only one curve for each is presented for clarity). The presence of graphene on top of the quartz further attenuates the propagating wave, which increases by 0.25 dB for single-layer graphene and 1.25 dB for the multilayer graphene. Also it must be noted that the phase in the measurement is basically constant regardless of the sample.

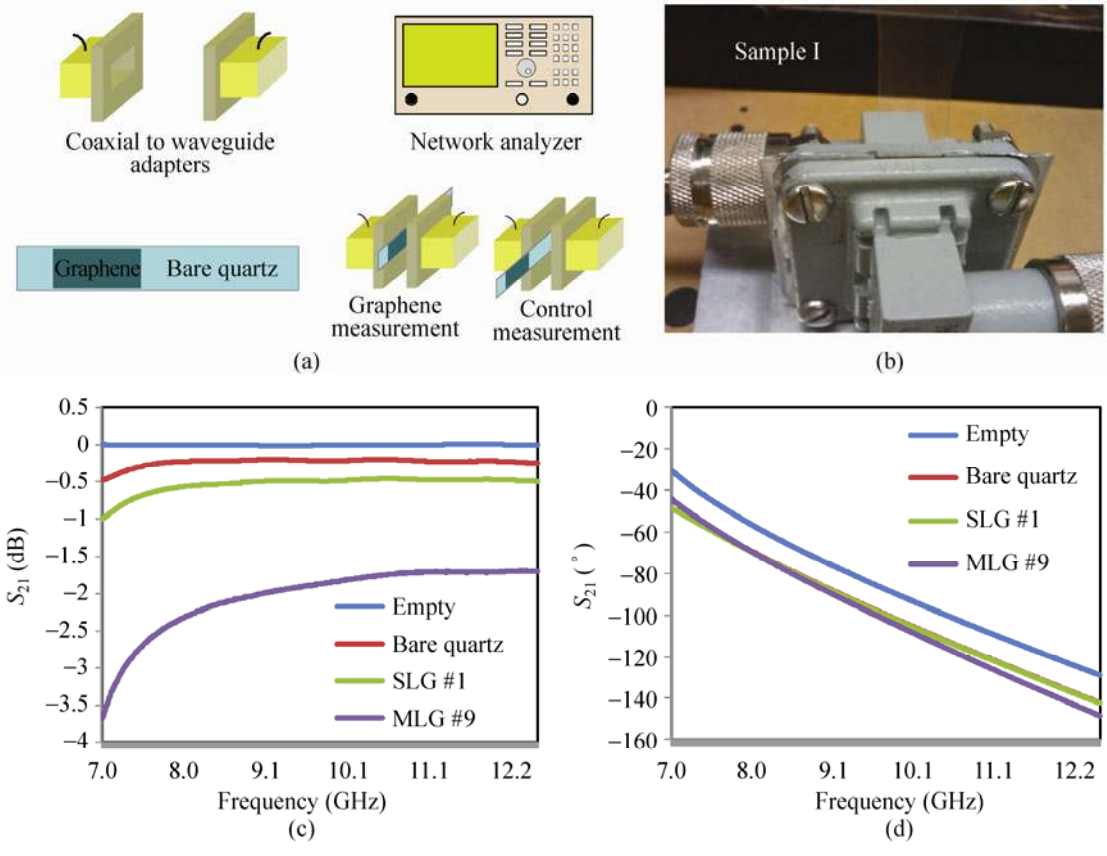

Figure 5 (a) Schematic view of measurement setup for X-band measurements, and (b) image of sample mounted inside waveguide, with bare quartz protruding. Comparison of the measured *S*-parameters for an empty waveguide, a reference bare quartz, and multilayer and single-layer samples of graphene (c) magnitude, (d) phase

To obtain the sheet resistance, Eq. (3) must be solved within the waveguide. This implies that guided quantities corresponding to the fundamental mode in the waveguide (TE_{10}) must be used for the wavenumber of the quartz substrate (k_Q) and the guided wave impedances for air and quartz substrates respectively ($Z_{0,Q}$),

$$Z_{0,Q} = \frac{\eta_0}{\sqrt{\varepsilon_{r0,Q} - \left(\frac{f_C}{f}\right)^2}}, k_Q = k\sqrt{\varepsilon_{rQ} - \left(\frac{f_C}{f}\right)^2} \quad (4)$$

where $\eta_0 = 120\pi$ is the free-space wave impedance and k is the free-space wavenumber.

Figure 6 displays the sheet resistance for multilayer (a) and single-layer graphene (b). For the multilayer samples, the sheet resistance is much lower than for the single-layer samples because of the additional parallel layers.

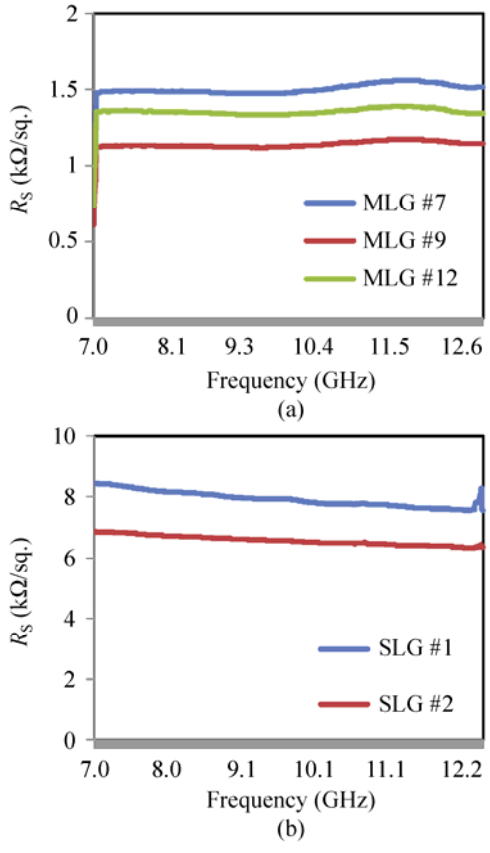

Figure 6 Measured sheet resistance of graphene on top of quartz at X-band: (a) multilayer; (b) single-layer

4. mm-Wave frequency characterization (W-band)

As opposed to the X-band, the dimensions in the W-band are compatible with a free-space transmission scheme for the present samples. To improve the signal-to-noise ratio (SNR) of the received signal and reduce the scattered field from surrounding clutter, two lenses were used to focus the beam to a spot size less than the width of the sample. For each graphene sample there are two additional control measurements, free space and bare quartz. The samples are measured in a wide frequency range from 75 GHz to 110 GHz using a programmable network analyzer (PNA) with external mm-wave headers (Fig. 7).

The dimensions of the samples allow us to take an image of the transmitted by means of a 2D linear stage moving in the focal plane. Due to the presence of the lenses, multiple reflections in the transmission path occur and these are present in the measured S_{21}. The signal must be filtered to separate the first arrival (without reflections from the setup) from the remaining reflections. Figure 8 presents the image of the magnitude and phase of the filtered S_{21} at 90 GHz, and it shows simultaneously the value for air, bare quartz substrate and multilayer graphene on top of quartz. It must be noted that the dimensions and position of the graphene sample on the substrate are easily identified (see Fig. 8(c) for a photograph of the sample location). After processing S_{21} measurements using Eq. (3), the sheet resistance of Fig. 9 is obtained.

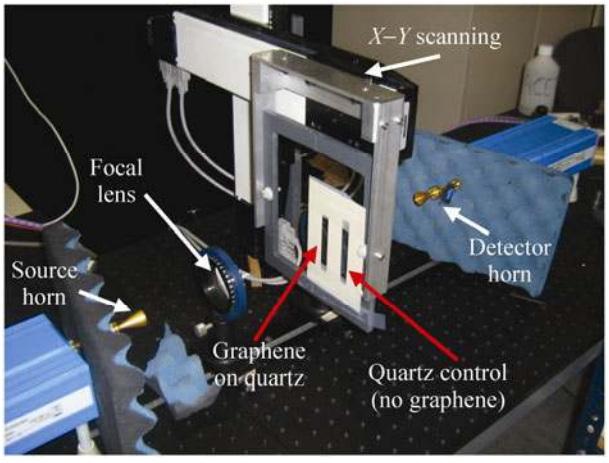

Figure 7 Picture of X-band imaging and quasi-optic transmission apparatus

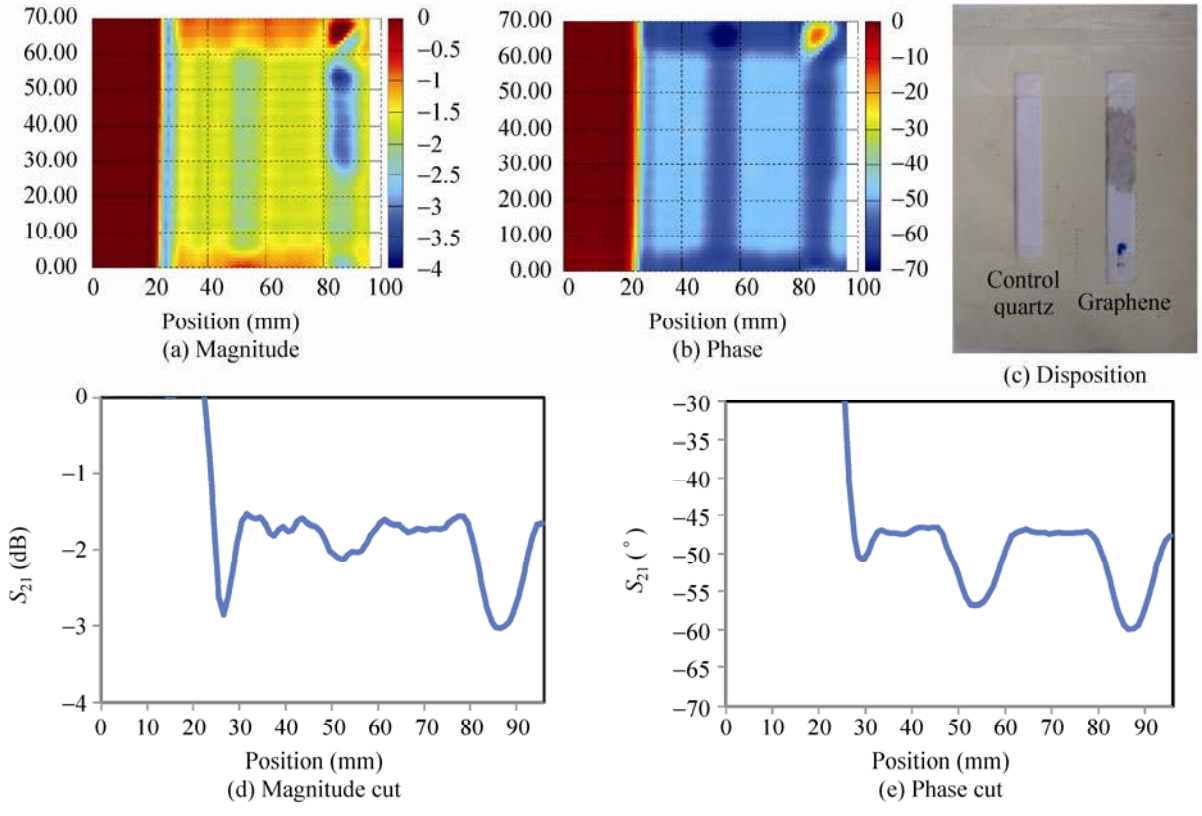

Figure 8 2D image of the measurement (MLG #9) at 90 GHz for the transmitted S_{21} through a bare quartz substrate, multilayer graphene and air. Magnitude data in dB; phase in degrees

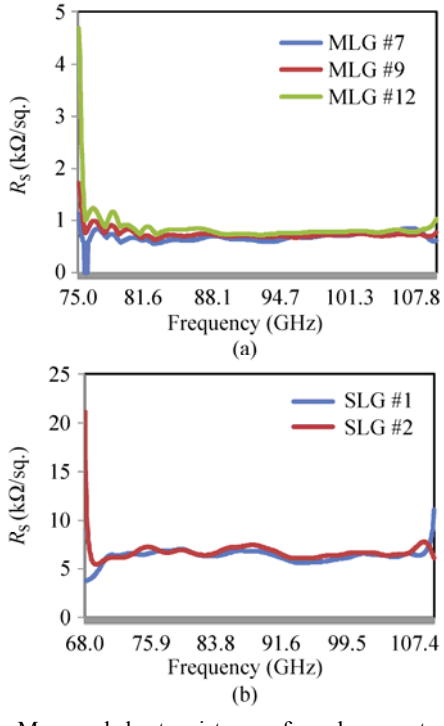

Figure 9 Measured sheet resistance of graphene on top of quartz at W-band: (a) multilayer (MLG); (b) single-layer (SLG)

5. THz frequency characterization

The THz measurements were performed in an optical setup using a coherent (homodyne) photomixing spectrometer with one photomixer as the THz transmitter, and a separate photomixer as the THz receiver. The system provides continuous tunable transmission measurement from 100 GHz to 1 THz with over 60 dB signal to noise in one sweep. The system is described in detail in Refs. [38–40]. This unique technique has never before been applied before to graphene films. The THz radiation is in the form of a Gaussian beam of focused width ~1 mm^2, and the angle of incidence is at or near perpendicular, allowing the Airy transmission formula to be used. The formula is [41]

$$T = \frac{8n^2}{A + B\cos(2kl) + C\sin(2kl)} \quad (5)$$

where

$$A = n^4 + 6n^2 + 1 + 2(n^2+1)g + (n^2+1)(b^2+g^2),$$
$$B = 2(n^2-1)g - (n^2-1)^2 + (n^2-1)(b^2+g^2),$$
$$C = 2(n^2+1)nb, \quad (6)$$
$$k = n\frac{\omega}{c}$$

and $y = g - ib = YZ_0 = (G - iB)Z_0 = (\sigma_1 - i\sigma_2)dZ_0$ is the dimensionless complex admittance per square of the film in units of the admittance Z_0^{-1} of free space (1/377 S). In this work b is neglected in comparison to g.

In Fig. 10, we plot the measured THz transmission data for the multilayer (a) and single-layer (b) samples. Because a quartz substrate of thickness 500 μm is used, the fringes in the transmission are visible in the raw transmission data. This allows us to accurately determine the index of refraction of quartz, and the quartz thickness, using a curve fit of Eq. (5). The value of n so found is 1.93, and the thickness 562 μm, close to the estimated values. Once these are determined, the sheet conductivity can be determined, again using Eq. (5). For the multilayer graphene, we are able to reliably extrapolate the sheet resistance. However, for the single-layer graphene, the calibration is not sufficient to show the difference between graphene and an open circuit (see the ESM for details). We can only put an upper bound of 0.1 mS on the sheet conductance of graphene in this frequency range. The entire set of data from the three different frequency bands is plotted for representative samples in Fig. 11.

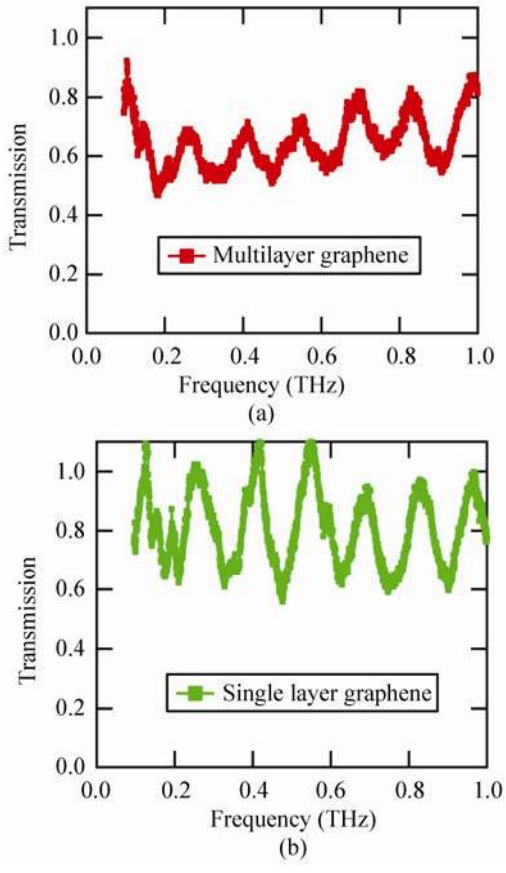

Figure 10 Plots of normalized transmission vs. frequency for single-layer and multilayer graphene

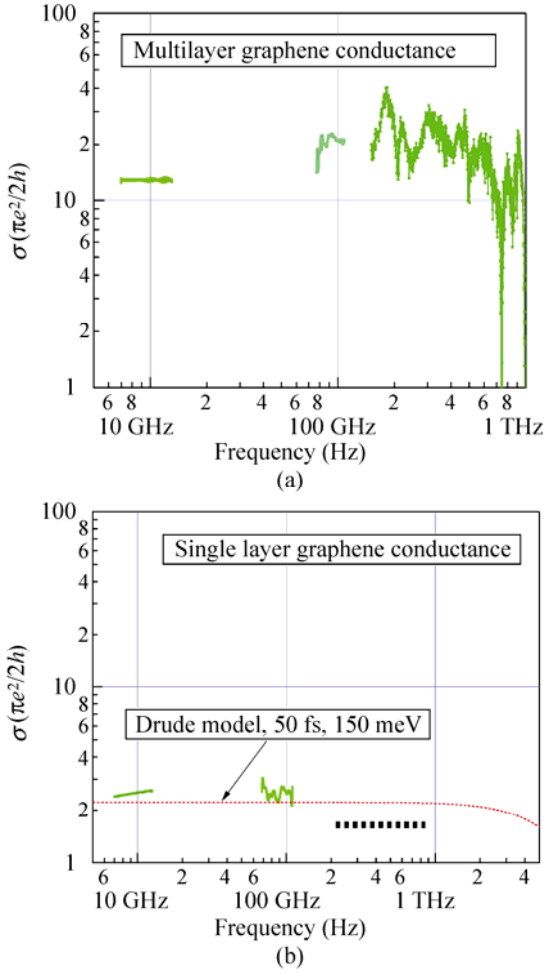

Figure 11 Plots of normalized conductance vs. frequency across all three bands (X band, W band, and THz) for (a) multilayer, and (b) single-layer samples. The black dashed line represents an upper limit on the single-layer measurement (see the ESM)

6. Discussion

The theoretical ac sheet conductance of single-layer graphene is $e^2/4\hbar$ and universal at optical frequencies,

but not at THz frequencies. The THz conductance is predicted to have a non-trivial dependence on temperature, scattering rate, Fermi energy, and frequency, and is given by [29]

$$\sigma(\omega)=\sigma^{\text{intra}}(\omega)+\sigma^{\text{inter}}(\omega) \tag{7}$$

$$\text{Re}\,\sigma^{\text{inter}}(\omega)=\frac{e^2}{4\hbar}\frac{\sinh(\omega/2k_{\text{B}}T)}{\cosh(E_{\text{F}}/k_{\text{B}}T)+\cosh(\omega/2k_{\text{B}}T)} \tag{8}$$

$$\text{Re}\,\sigma^{\text{intra}}(\omega)=\frac{e^2}{4\hbar}\frac{8}{\pi}\frac{k_{\text{B}}T\tau/(2\pi\hbar)}{1+(\omega\tau)^2}\ln\left(2\cosh\left(\frac{E_{\text{F}}}{2k_{\text{B}}T}\right)\right) \tag{9}$$

where T is the temperature, E_{F} the Fermi energy, and τ the scattering time ($1/\Gamma$). In the presence of many-body (electron–electron) interactions, this may require augmentation [42]. Physically, the interband term corresponds to electron–hole pair generation and recombination events. Numerically, due to thermal smearing, this term is expected to be $\ll e^2/4\hbar$ for frequencies < 1 THz, even if the Fermi energy is zero, and is thus not considered further in our analysis.

Physically, the intraband term corresponds to free-carrier conductivity. For the present experiments, the temperature is finite but below $E_{\text{F}}/k_{\text{B}}$, so that this can be approximated as

$$\text{Re}\,\sigma^{\text{intra}}(\omega)=\frac{e^2}{4\hbar}\frac{4}{\pi}\frac{E_{\text{F}}\tau/(2\pi\hbar)}{1+(\omega\tau)^2} \tag{10}$$

The typical values of the Fermi energy are between 100 to 500 meV, and the scattering time (at least from DC measurements) has been determined to be between 10 and 500 fs for exfoliated graphene at low temperatures [43]. The corresponding DC mobility is between 1000 and 20 000 cm^2/(V·s) and so can be expected to be representative of moderate to very high quality SLG. We can use these parameters to project the THz properties of graphene, as shown in Fig. 12. Based on these projections, we find that our SLG (with E_{Fermi} ~ 150 meV, see the ESM) has a scattering time of 50 fs. (this curve fit is shown in Fig. 11(b)). The SLG data are consistent with separate DC measurements on moderate mobility samples [43]. Given the size of these samples (~1 cm × 2.5 cm), it is not surprising that the scattering time (which is indicative of the mobility and quality of the graphene sheet) is not as large as the cleanest sheets reported in the literature, which typically are about six orders of magnitude smaller in area (~10 μm × 10 μm) [44]. Thus, clearly, future research will be needed to develop cm-scale SLG samples with large scattering times, high mobility, and high material quality, comparable to the best quality graphene microscopic flakes. Very recent efforts in this area are very promising [45]. With such improved mobility and higher Fermi energy, the sheet conductivity can be modulated to even larger values, which we address next.

In Fig. 12, we have generated a series of theoretical curves that represent gradually increasing values of the Fermi energy (and hence electron density) from 0.1 to 0.5 eV, corresponding to commonly achieved electron sheet concentrations in the range 1×10^{12}–10×10^{12} cm^{-2}. Increasing the density also decreases the scattering rate [43], and hence in these curves we have also increased the scattering time from 60 fs to 510 fs (using Eq. (10)). The Fermi energy is straightforward to modulate with the appropriate gating structure, which we are currently investigating experimentally (to be published at a later date). In these first generation single-layer graphene THz measurements, the scattering time of these samples (50 fs) corresponds to a moderate quality graphene layer, hence the sheet conductivity of the SLG is ~$2e^2/4\hbar$ over the frequency range measured. In the future, increased mobility

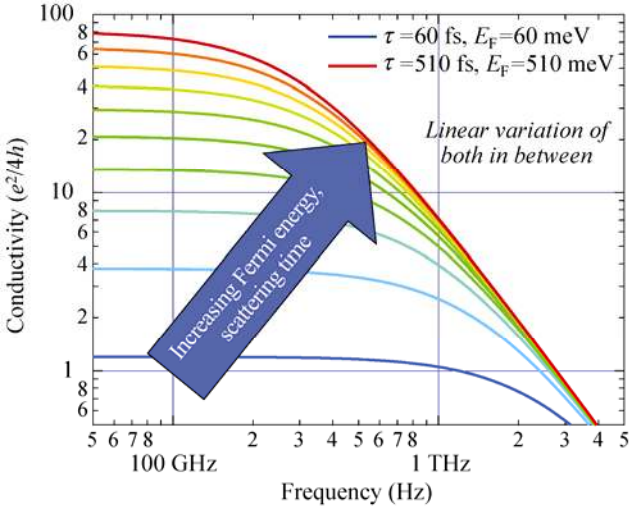

Figure 12 Projected normalized sheet conductance vs. frequency for increasing values of E_{Fermi} and τ, from 60 to 510 meV and 60 to 510 fs, respectively

devices coupled with gating structures can give rise to a voltage tunable THz spatial-light modulators, which would be a technologically significant electro-optic device for THz optics and systems. Note especially that the sheet resistance can be tuned right around the optimum sensitivity for modulators, the characteristic impedance of free space 377 Ω, which is $40e^2/4\hbar$. Thus, this is the first step towards THz graphene optics.

We now turn to a comparison of our data to prior art in the field for CW THz graphene measurements. In Fig. 13, we plot the data from three references: Ours, IBM [5], and Berkeley [3, 4]. For the data band measured, none of the groups completely maps the Drude rolloff. Our data are below the rolloff, whereas the data of IBM and Berkeley are above the rolloff. Therefore, future work with either higher mobility graphene in the THz band, or a combination of THz and FTIR, are required to completely map the transition through the Drude scattering time.

Turning to the multilayer data, a comprehensive theory of the Drude response in MLG is currently not available. Thus, the MLG sample is not expected to behave exactly according to the Drude model. However, prior optical and IR work [8] have shown that the coupling between layers is relatively unimportant for the IR properties, and that over most of the spectral range, the sheets behave as independent sheets in parallel. Our measurements, which are the first on MLG in this band, qualitatively corroborate this interpretation: The sheet conductance for our MLG samples is ~5–10 times larger than the SLG over the entire band (Fig. 11). The MLG data show a significant difference between the 10 GHz and 100 GHz sheet conductance, which we presently do not have an explanation for. Manipulating the number of layers clearly opens another potential degree of freedom for THz graphene optics.

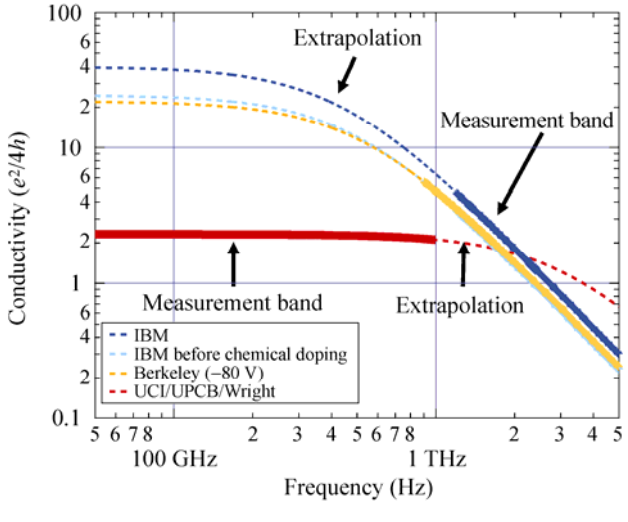

Figure 13 Comparison of conductivity vs. frequency plots with prior work; solid lines are from measured bands and the dotted lines are the extrapolated data. UCI refers to all data ⩽ 1 THz, IBM [5] and Berkeley [3, 4] refer to all data > 1 THz

Our work has focused mostly on the absorptive (real) component of the graphene impedance, as measurements of the absorption are most straightforward. However, the imaginary impedance can have many important applications in the future, allowing wave-guiding, sub-wavelength manipulation of THz waves, metamaterials, and more generally, graphene plasmonics [46]. Our microwave measurement technique clearly has the ability to infer the phase of the transmitted wave as well as the amplitude, and efforts are under way by one of us (E. Brown) to extend this concept of phase-sensitive measurements to THz photomixing spectrometry. These exciting new techniques will give us new and unprecedented opportunities to investigate, manipulate, and exploit the unique properties of 2D materials in THz devices and systems.

7. Conclusion

We have presented the first absolute measurement of the conductance of both SLG and MLG in the technologically important RF frequency range between 10 GHz and 1 THz, finding a value between 2 $e^2/4\hbar$ (SLG) and 20 $e^2/4\hbar$ (MLG). This is consistent with graphene having excess AC conductivity above the optical (interband) value, likely an intraband component whose contribution depends on the Fermi level and scattering time, estimated to be 50 fs. The MLG samples behave as independent layers in parallel. Based on these measurements, simulations of device performance suggest that a very useful modulation of the conductivity and transparency is possible using gated structures on high-quality graphene material. Taken collectively, these results establish a strong

support for applications of graphene in the microwave, mm-wave, and THz range.

Acknowledgements

This work was funded by the Army Research Office (MURI W911NF-11-1-0024, ARO W911NF-09-1-0319, and DURIP W911NF-11-1-0315) and by Ministerio de Educación y Ciencia (FPU and Consolider CSD2008-0068).

Electronic Supplementary Material: Supplementary material (further details of the transfer technique and fabrication process, graphene quality, analysis of number of layers, optical and AFM imaging, Raman spectroscopy, modeling and formulation, calibration, measurements, and statistical analysis) is available in the online version of this article at http://dx.doi.org/10.1007/s12274-012-0251-0.

References

[1] Nair, R. R.; Blake, P.; Grigorenko, A. N.; Novoselov, K. S.; Booth, T. J.; Stauber, T.; Peres, N. M. R.; Geim, A. K. Fine structure constant defines visual transparency of graphene. *Science* **2008**, *320*, 1308.

[2] Li, Z.; Henriksen, E.; Jiang, Z.; Hao, Z.; Martin, M.; Kim, P.; Stormer, H.; Basov, D. Dirac charge dynamics in graphene by infrared spectroscopy. *Nat. Phys.* **2008**, *4*, 532–535.

[3] Horng, J.; Chen, C. F.; Geng, B.; Girit, C.; Zhang, Y.; Hao, Z.; Bechtel, H. A.; Martin, M.; Zettl, A.; Crommie, M. F. Drude conductivity of Dirac fermions in graphene. *Phys. Rev. B* **2011**, *83*, 165113.

[4] Ju, L.; Geng, B.; Horng, J.; Girit, C.; Martin, M.; Hao, Z.; Bechtel, H. A.; Liang, X.; Zettl, A.; Shen, Y. R., et al. Graphene plasmonics for tunable terahertz metamaterials. *Nat. Nanotechnol.* **2011**, *6*, 630–634.

[5] Yan, H.; Xia, F.; Zhu, W.; Freitag, M.; Dimitrakopoulos, C.; Bol, A. A.; Tulevski, G.; Avouris, P. Infrared spectroscopy of wafer-scale graphene. *ACS Nano* **2011**, *5*, 9854–9860.

[6] Tomaino, J. L.; Jameson, A. D.; Kevek, J. W.; Paul, M. J.; van der Zande, A. M.; Barton, R. A.; McEuen, P. L.; Minot, E. D.; Lee, Y. -S. Terahertz imaging and spectroscopy of large-area single-layer graphene. *Opt. Express* **2011**, *19*, 141–146.

[7] Liu, W.; Aguilar, R. V.; Hao, Y. F.; Ruoff, R. S.; Armitage, N. P. Broadband microwave and time-domain terahertz spectroscopy of chemical vapor deposition grown graphene. *J. Appl. Phys.* **2011**, *110*, 083510.

[8] Kuzmenko, A. B.; van Heumen, E.; Carbone, F.; van der Marel, D. Universal optical conductance of graphite. *Phys. Rev. Lett.* **2008**, *100*, 117401.

[9] Mak, K. F.; Sfeir, M. Y.; Misewich, J. A.; Heinz, T. F. The evolution of electronic structure in few-layer graphene revealed by optical spectroscopy. *P. Natl. Acad. Sci. USA* **2010**, *107*, 14999–15004.

[10] Dawlaty, J. M.; Shivaraman, S.; Strait, J.; George, P.; Chandrashekhar, M.; Rana, F.; Spencer, M. G.; Veksler, D.; Chen, Y. Measurement of the optical absorption spectra of epitaxial graphene from terahertz to visible. *Appl. Phys. Lett.* **2008**, *93*, 131905.

[11] Choi, H.; Borondics, F.; Siegel, D. A.; Zhou, S. Y.; Martin, M. C.; Lanzara, A.; Kaindl, R. A. Broadband electromagnetic response and ultrafast dynamics of few-layer epitaxial graphene. *Appl. Phys. Lett.* **2009**, *94*, 172102.

[12] Kim, J. Y.; Lee, C.; Bae, S.; Kim, K. S.; Hong, B. H.; Choi, E. Far-infrared study of substrate-effect on large scale graphene. *Appl. Phys. Lett.* **2011**, *98*, 201907.

[13] Krupka, J.; Strupinski, W. Measurements of the sheet resistance and conductivity of thin epitaxial graphene and SiC films. *Appl. Phys. Lett.* **2010**, *96*, 082101.

[14] Krupka, J.; Strupinski, W.; Kwietniewski, N. Microwave conductivity of very thin graphene and metal films. *J. Nanosci. Nanotechnol.* **2011**, *11*, 3358–3362.

[15] Skulason, H.; Nguyen, H.; Guermoune, A.; Sridharan, V.; Siaj, M.; Caloz, C.; Szkopek, T. 110 GHz measurement of large-area graphene integrated in low-loss microwave structures. *Appl. Phys. Lett.* **2011**, *99*, 153504.

[16] Kundhikanjana, W.; Lai, K.; Wang, H.; Dai, H.; Kelly, M. A.; Shen, Z. Hierarchy of electronic properties of chemically derived and pristine graphene probed by microwave imaging. *Nano Lett.* **2009**, *9*, 3762–3765.

[17] Talanov, V. V.; Barga, C. D.; Wickey, L.; Kalichava, I.; Gonzales, E.; Shaner, E. A.; Gin, A. V.; Kalugin, N. G. Few-layer graphene characterization by near-field scanning microwave microscopy. *ACS Nano* **2010**, *4*, 3831–3838.

[18] Rana, F. Graphene terahertz plasmon oscillators. *IEEE T. Nanotechnol.* **2008**, *7*, 91–99.

[19] Burke, P. J.; Spielman, I. B.; Eisenstein, J. P.; Pfeiffer, L. N.; West, K. W. High frequency conductivity of the high-mobility two-dimensional electron gas. *Appl. Phys. Lett.* **2000**, *76*, 745–747.

[20] Allen, S. J.; Tsui, D. C.; Logan, R. A. Observation of

Note added in proof: During the preparation of this manuscript we became aware of similar work showing modulation of the ~0.5 THz transmission of graphene as projected in Section 6 of this manuscripts in Refs. [47–48].

2-dimensional plasmon in silicon inversion layers. *Phys. Rev. Lett.* **1977**, *38*, 980–983.

[21] Kang, S.; Burke, P.; Pfeiffer, L.; West, K. Resonant frequency response of plasma wave detectors. *Appl. Phys. Lett.* **2006**, *89*, 213512.

[22] Dragoman, M.; Muller, A.; Dragoman, D.; Coccetti, F.; Plana, R. Terahertz antenna based on graphene. *J. Appl. Phys.* **2010**, *107*, 104313.

[23] Burke, P. J.; Li, S. D.; Yu, Z. Quantitative theory of nanowire and nanotube antenna performance. *arXiv: cond-mat/0408418v1* **2004**.

[24] Burke, P. J.; Li, S. D.; Yu, Z. Quantitative theory of nanowire and nanotube antenna performance. *IEEE T. Nanotechnol.* **2006**, *5*, 314–334.

[25] Hanson, G. W. Fundamental transmitting properties of carbon nanotube antennas. *IEEE T. Antenn. Propag.* **2005**, *53*, 3426–3435.

[26] Slepyan, G. Y.; Shuba, M. V.; Maksimenko, S. A.; Lakhtakia, A. Theory of optical scattering by achiral carbon nanotubes and their potential as optical nanoantennas. *Phys. Rev. B* **2006**, *73*, 195416.

[27] Russer, P.; Fichtner, N.; Lugli, P.; Porod, W.; Russer, J. A.; Yordanov, H. Nanoelectronics-based integrated antennas. *IEEE Microw. Mag* .**2010**, *11*, 58–71.

[28] Shuba, M. V.; Paddubskaya, A. G.; Plyushch, A. O.; Kuzhir, P. P.; Slepyan, G. Y.; Maksimenko, S. A.; Ksenevich, V. K.; Buka, P.; Seliuta, D.; Kasalynas, I., et al. Experimental evidence of localized plasmon resonance in composite materials containing single-wall carbon nanotubes. *Phys. Rev. B* **2012**, *85*, 165435.

[29] Falkovsky, L. A. Optical properties of graphene and Ⅳ–Ⅵ semiconductors. *Phys.-Usp.* **2008**, *51*, 887–897.

[30] Gusynin, V.; Sharapov, S.; Carbotte, J. On the universal ac optical background in graphene. *New J. Phys.* **2009**, *11*, 095013.

[31] Li, X.; Cai, W.; An, J.; Kim, S.; Nah, J.; Yang, D.; Piner, R.; Velamakanni, A.; Jung, I.; Tutuc, E., et al. Large-area synthesis of high-quality and uniform graphene films on copper foils. *Science* **2009**, *324*, 1312–1314.

[32] Lenski, D. R.; Fuhrer, M. S. Raman and optical characterization of multilayer turbostratic graphene grown via chemical vapor deposition. *J. Appl. Phys.* **2011**, *110*, 013720.

[33] Li, X.; Zhu, Y.; Cai, W.; Borysiak, M.; Han, B.; Chen, D.; Piner, R. D.; Colombo, L.; Ruoff, R. S. Transfer of large-area graphene films for high-performance transparent conductive electrodes. *Nano Lett.* **2009**, *9*, 4359–4363.

[34] Barroso, J. J.; Castro, P. J.; Leite Neto, J. P. Electrical conductivity measurement through the loaded Q factor of a resonant cavity. *Int. J. Infrared Milli.* **2003**, *24*, 79–86.

[35] Ceremuga-Mazierska, J. Transmission of microwave signals through superconducting thin films in waveguides. *Supercond. Sci. Tech.* **1992**, *5*, 391.

[36] Balanis, C. A. *Advanced engineering electromagnetics;* Wiley: New York, 1989.

[37] Rugheimer, N.; Lehoczky, A.; Briscoe, C. Microwave transmission-and reflection-coefficient ratios of thin superconducting films. *Phys. Rev.* **1967**, *154*, 414–421.

[38] Brown, E. R.; Bjarnason, J.; Chan, T. L. J.; Driscoll, D. C.; Hanson, M.; Gossard, A. C. Room temperature, THz photomixing sweep oscillator and its application to spectroscopic transmission through organic materials. *Rev. Sci. Instrum.* **2004**, *75*, 5333–5342.

[39] Demers, J. R.; Logan, R. T.; Bergeron, N. J.; Brown, E. R. A high signal-to-noise ratio, coherent, frequency-domain THz spectrometer employed to characterize explosive compounds. In *33rd International Conference on Infrared, Millimeter and Terahertz Waves, IRMMW-THz*, California, USA, 2008, pp. 1–3.

[40] Brown, E.; Mendoza, E. A.; Xia, D.; Brueck, S. Narrow THz spectral signatures through an RNA solution in nanofluidic channels. *IEEE Sens. J.* **2010**, *10*, 755–759.

[41] Glover, R. E.; Tinkham, M. Conductivity of superconducting films for photon energies between 0.3 and 40 kT_c. *Phys. Rev.* **1957**, *108*, 243–256.

[42] Abedinpour, S. H.; Vignale, G.; Principi, A.; Polini, M.; Tse, W. K.; MacDonald, A. Drude weight, plasmon dispersion, and ac conductivity in doped graphene sheets. *Phys. Rev. B* **2011**, *84*, 045429.

[43] Tan, Y. W.; Zhang, Y.; Bolotin, K.; Zhao, Y.; Adam, S.; Hwang, E.; Das Sarma, S.; Stormer, H.; Kim, P. Measurement of scattering rate and minimum conductivity in graphene. *Phys. Rev. Lett.* **2007**, *99*, 246803.

[44] Chen, J.; Jang, C.; Xiao, S.; Ishigami, M.; Fuhrer, M. Intrinsic and extrinsic performance limits of graphene devices on SiO_2. *Nat. Nanotechnol.* **2008**, *3*, 206–209.

[45] Shen, T.; Wu, W.; Yu, Q.; Richter, C. A.; Elmquist, R.; Newell, D.; Chen, Y. P. Quantum Hall effect on centimeter scale chemical vapor deposited graphene films. *Appl. Phys. Lett.* **2011**, *99*, 232110.

[46] Koppens, F. H. L.; Chang, D. E.; García de Abajo, F. J. Graphene plasmonics: A platform for strong light–matter interactions. *Nano Lett.* **2011**, *11*, 3370–3377.

[47] Sensale-Rodriguez, B.; Yan, R.; Kelly, M. M.; Fang, T.; Tahy, K.; Hwang, W. S.; Jena, D.; Liu, L.; Xing, H. G. Broadband graphene terahertz modulators enabled by intraband transitions.*Nat. Commun.* **2012**, *3*: 780.

[48] Sensale-Rodriguez, B.; Yan, R.; Rafique, S.; Zhu, M.; Li, W.; Liang, X. L.; Gundlach, D.; Protasenko, V.; Kelly, M. M.; Jena, D.; Liu, L.; Xing, H. G. Extraordinary Control of Terahertz Beam Reflectance in Graphene Electro-absorption Modulators.*Nano Lett.* **2012**, *9*: 4518–4522

Electronic Supplementary Material

Terahertz Graphene Optics

Nima Rouhi[1], Santiago Capdevila[2], Dheeraj Jain[1], Katayoun Zand[1], Yung Yu Wang[1], Elliott Brown[3], Lluis Jofre[2], and Peter Burke[1] (✉)

[1] Integrated Nanosystems Research Facility, Department of Electrical Engineering and Computer Science, University of California, Irvine, CA 92697, USA
[2] Universitat Politècnica de Catalunya, Barcelona, Spain
[3] Wright State University, Dayton, OH 45435, USA

Supporting information to DOI 10.1007/s12274-012-0251-0

Graphene growth and transfer

Multilayer graphene was grown on nickel film deposited on top of Si/SiO_2 substrates using the chemical vapor deposition (CVD) method [1]. Single-layer graphene was grown on copper foils using CVD [2]. The transfer process was almost the same for both samples. Poly(methyl methacrylate) (PMMA) was spin-coated on the sample (3500 rpm for 60 s), and then samples were pre-baked on hot plate at 190 ˚C. Copper foil (or nickel for multilayer graphene samples) was wet etched ($FeCl_3$ for the Cu and HCl for the Ni) until no residue of the metal was observed on the sample leaving graphene/PMMA floating on the etchant. Samples were then transferred and left in deionized (DI) water for 2 hours. DI water was changed again and left for another 3–5 hours (or overnight in some cases) to get rid of the etchant residues on graphene films. Next, graphene/PMMA films were transferred to the target substrate (quartz in this case). Subsequently, another layer of PMMA was coated on the sample and dried out so that fewer defects were introduced in the PMMA removal step. Following that, samples were left in warm acetone for 2–3 hours and then transferred to a fresh acetone bath and left for additional 2 hours to remove the PMMA completely from the sample leaving graphene films on top of quartz substrates. Consistent with other work, residual PMMA was not completely removed by the acetone soak. It is anticipated that future work with an annealing step may yield higher mobility samples. However, the uniformity of doping seems reasonable, as characterized below.

Counting the number of layers

Optical imaging, Raman spectroscopy, and atomic force microscopy (AFM) were used to count the number of layers in each sample (Fig. S-1). Since optical images of graphene sheets on quartz substrate were not clear enough, we used the same batch of graphene samples with the exact same transfer process to deposit graphene on Si/SiO_2 substrates for optical imaging purposes. We estimated the number of layers to be in the range of 3 to 7 layers for our graphene films grown on Ni. Based on the Raman spectrum, the G/2D peak intensity ratio was calculated to help us with counting the number of layers [3–8]. Counting layers requires a more detailed study then merely the G/2D peak ratio. Therefore we also used AFM and optical imaging to validate our data. However, the exact number of layers in multilayer samples with more than five layers of graphene is hard to

Address correspondence to pburke@uci.edu

obtain. To precisely acquire the G/2D peak intensity ratio, around 20 random spots (in a 1 cm × 1 cm area) were analyzed to obtain the Raman spectrum. The full-width half-maximum of the 2D peak for multilayer samples was found to be ~80 cm^{-1} and the average intensity ratio $I_{(G)}/I_{(2D)}$ was around 1.2.

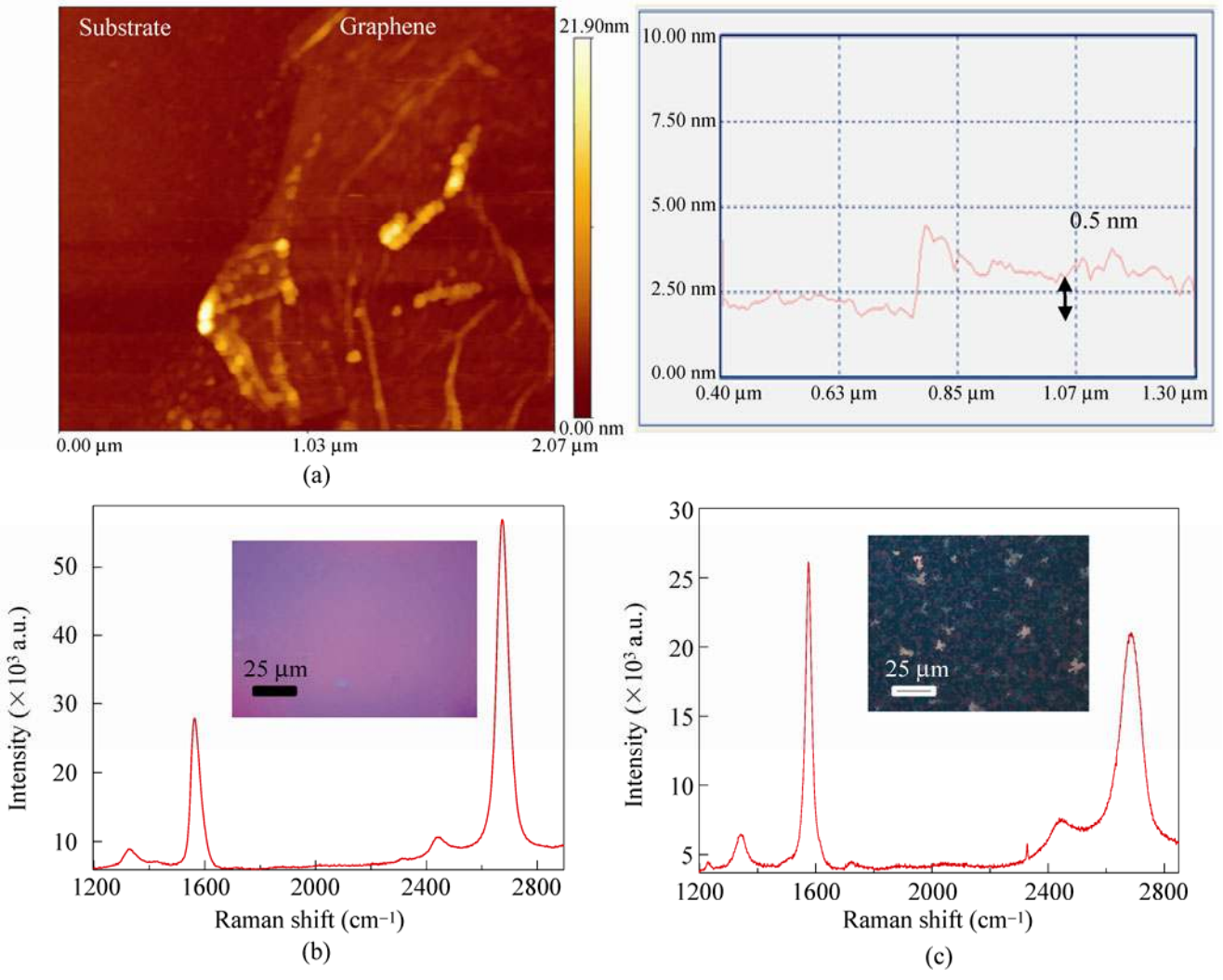

Figure S-1 (a) AFM image and height data for a single-layer graphene sample. Raman spectrum of graphene films grown on (b) Cu, and (c) Ni. The insets in b and c respectively show optical images of single-layer and multilayer graphene on Si substrates

On the other hand, LPCVD graphene grown on Cu foil is known to result in more than 90% single-layer graphene coverage over the sample On the other hand, LPCVD graphene grown on Cu foil is known to result in more than 90% single-layer graphene coverage over the sample [2, 9], as opposed to AP-CVD grown graphene on copper which is known to have significant turbostratic and multilayer areas [10]. This is clearly not the case in our LPCVD Cu-grown samples. Unlike multilayer graphene, in single-layer graphene films the 2D peak (~2680 nm) is sharper and more intense compared to the G peak (~1580 nm). Similar to multilayer analysis, here in single-layer graphene samples we also used Raman, AFM, and optical imaging to confirm number of layers [9, 11] as can be seen in Figs. S-1 and S-3. The full-width half-maximum of the 2D peak of single-layer graphene was ~47 cm^{-1}. Based on the Raman spectrum analysis, AFM data, and optical images extracted from our samples with LPCVD grown graphene on Cu, the quartz substrate was considered to be mostly covered by one layer of graphene with some areas having two or three layers.

The uniformity of the single-layer graphene (SLG) sample is confirmed by studying Raman spectrum obtained from 11 random spots over the 1 cm × 1 cm area of the sample. Statistical results show a small range of $I_{(G)}/I_{(2D)}$ peak ratio variation (from 0.40 to 0.53, with one peak ratio around 1, which is not shown in histograms) with a concentration around the average ratio, 0.46 (Fig. S-2(a)). For MLG samples, (although they are all made of transferred graphene film from the same batch of graphene grown on Ni and cut in pieces), we aimed to investigate the uniformity from sample to sample. We plot a histogram of the $I_{(G)}/I_{(2D)}$ peak ratio for 19 random spots in a 1 cm × 1 cm area of three different multilayer samples (Fig. S-3(a)) demonstrating the distribution range of 0.85–1.6 in the peak ratio variation, mostly concentrated around the average ratio (1.2). According to the optical images and Raman data analysis, the samples are considered to be essentially uniform.

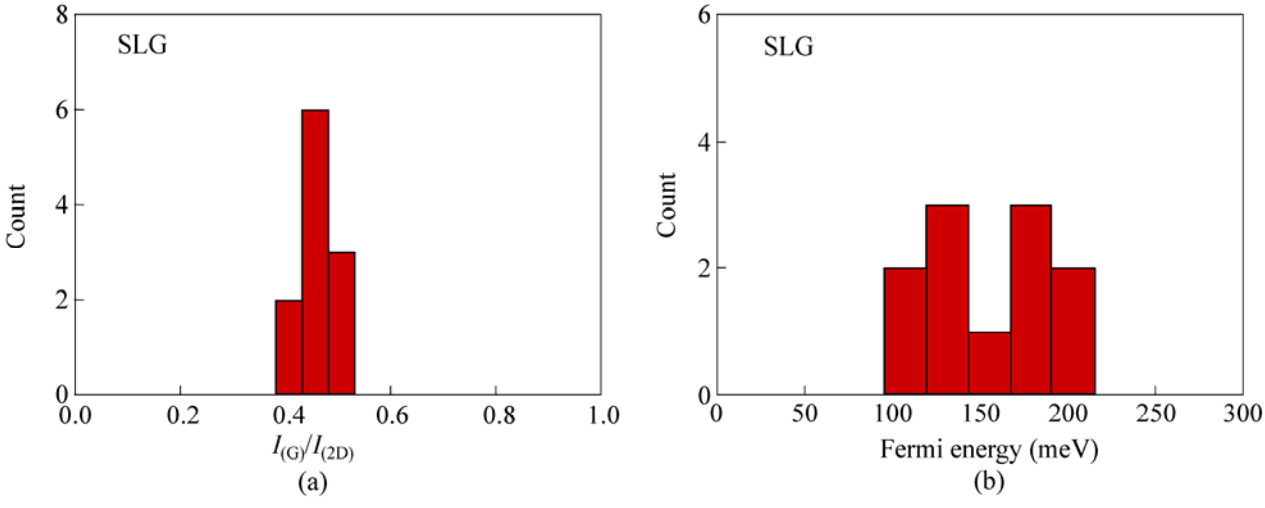

Figure S-2 (a) Statistical variation analysis of $I_{(G)}/I_{(2D)}$ peak ratio from 11 spots in a 1 cm × 1 cm area of an individual single-layer sample showing a small range (0.4–0.53) of peak ratio variation with uniform distribution over the range. (b) Fermi energy distribution based on G-peak shift relative to 1580 cm^{-1} for SLG samples

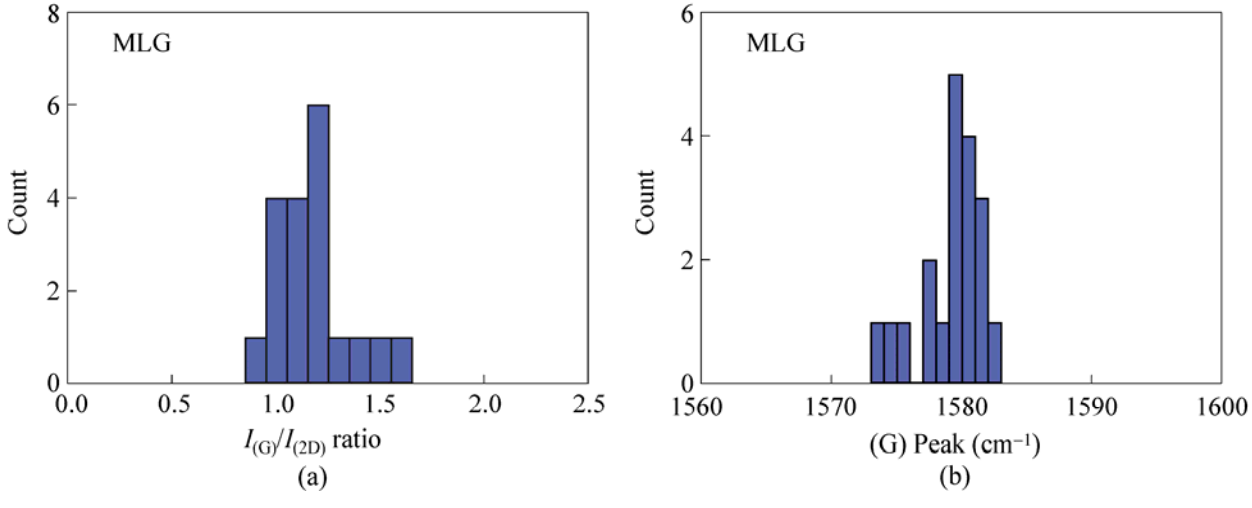

Figure S-3 (a) Histogram of $I_{(G)}/I_{(2D)}$ peak ratio for 19 spots in a 1 cm × 1 cm area of three different multilayer samples demonstrating the distribution range of 0.85–1.6 ratio, mostly concentrated around the average ratio (1.2). (b) G peak position histogram for 3 MLG samples within the range 1573–1582 cm^{-1} with a spike at the average (1579 cm^{-1})

On the other hand, the doping effect of residual PMMA (after acetone cleaning) can be mapped by the shift in G peak position. Based on the distribution results it can be seen that the range of G peak positions for SLG samples was from 1584–1588 cm^{-1} (Fig. S-2(b) shows the relative changes in Fermi energy based on G-peak shift). For three MLG samples the G peak variation range was from 1573–1582 cm^{-1} (Fig. S-3(b)). Apparently this insignificant variation change, especially for SLG sample, shows a minimal effect of residual PMMA after cleaning. As the samples are not gated, their doping is fixed. Based on the location of the G-band shift (relative to 1580 cm^{-1}), we estimate the sample to be p-doped with a Fermi energy of ~150 meV on average using a coefficient of 42 $cm^{-1} \cdot eV^{-1}$ [12].

TRL calibration (X-band)

We used the industry-standard thru-reflect-line (TRL) calibration for the waveguide junction. This requires measuring the microwave scattering parameters in the presence of a reflect termination (a short circuit has been used), a thru connection, and a quarter wavelength waveguide (at the central frequency), and computing and storing the calibration coefficients into a computer. Then, when the sample is measured, the raw S-parameters can be corrected applying the calibration coefficients, and the S-parameters are obtained at the reference plane of the sample, having removed the effects of the coaxial to waveguide transitions. Figure S-4 shows the short (reflect), thru, line, and two representative samples. Figure S-5 shows the raw measured S parameter data for SLG and MLG samples, as well as the control sample (quartz only, no graphene film), and the corrected S-parameter data after using the TRL calibration. The inferred film resistance for both samples is also plotted. Residual errors in the calibration, such as the presence of small standing waves and noise have been removed in the main text results applying a moving average filter.

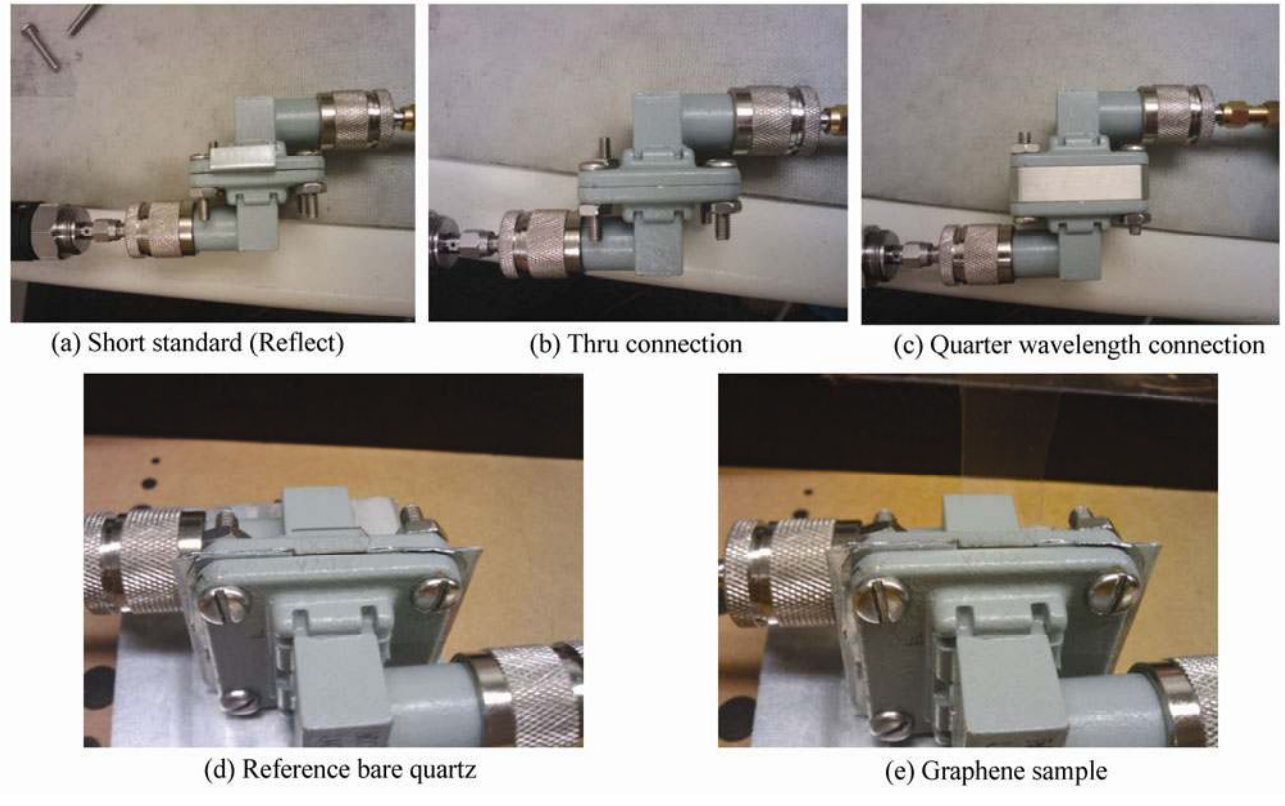

Figure S-4 TRL calibration standards (top), and control sample and graphene film mounted in waveguide (bottom)

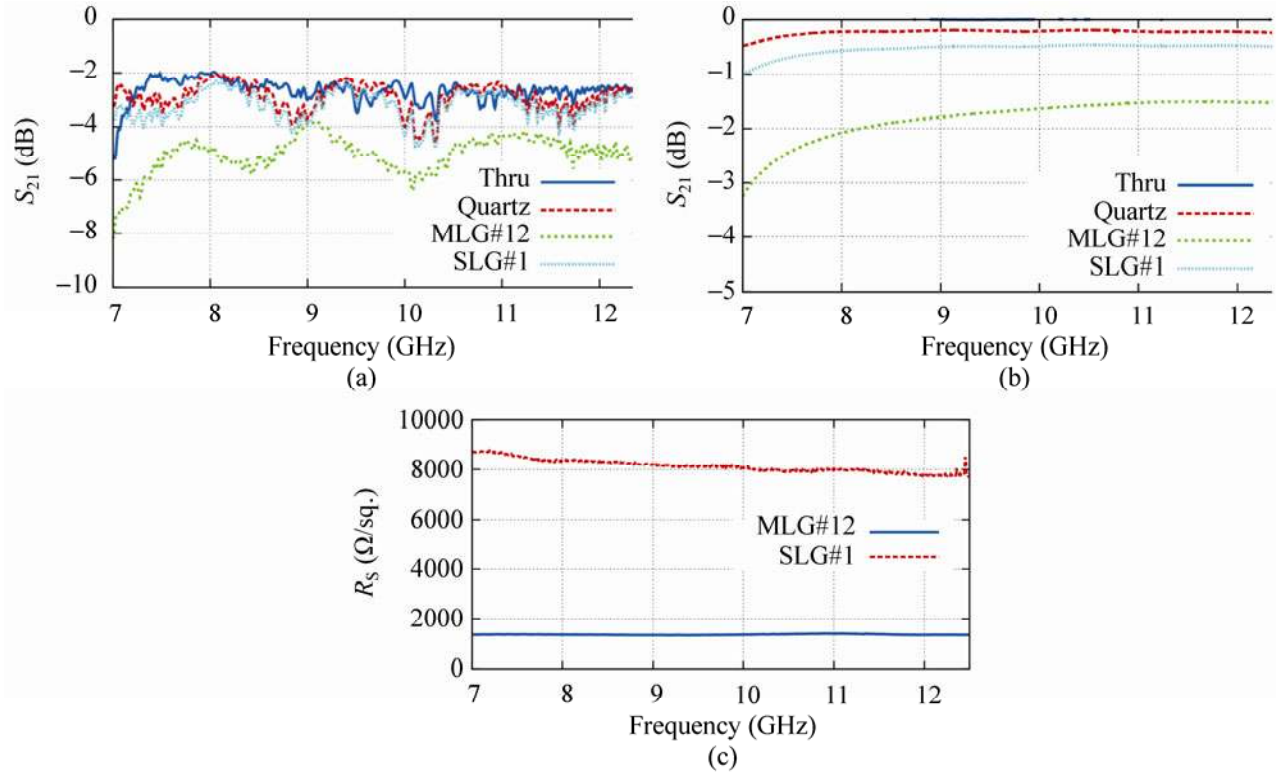

Figure S-5 (a) Raw measured microwave parameters; (b) Corrected (using TRL calibration technique) microwave transmission; (c) Sheet resistance determined using

Uncertainty analysis

The more important sources of error in the retrieval of the sheet resistance are the quartz thickness uncertainty and the noise level of the measurement, with some other sources such as the angle of incidence having a much lower impact. For the X-band measurement, since the thickness of the substrate is much smaller than the wavelength, its impact is not as large as for instance in the case of the W-band. Assuming an uncertainty in the quartz thickness of 10%, and a noise floor of the S_{21} parameter of –65dB (worst case scenario), the uncertainty in the retrieved sheet resistance is below 10% for X-band measurements and between 10 and 20% for W-band measurements.

Alternative formulation of RF modeling

Although the main text takes a multiple reflection point of view for the RF sheet conductance modeling, an alternative formulation based on impedance mismatch is also possible. In all of our RF experiments the radiation is CW coherent and we measure the normalized transmitted power (transmissivity) through the graphene-on-quartz sample as a function of frequency in the microwave, mm-wave, or THz regions. The radiation is also propagating perpendicular to the quartz substrate as a TE guided wave, or TEM free-space wave. Under these conditions, we can model the experimental transmissivity by the equivalent-circuit model shown in Fig. 3 and Fig. S-6. The incident power is represented in terms of an equivalent sinusoidal current generator i_s. The quartz substrate is represented by a uniform transmission line of physical length l and characteristic impedance $Z_Q = \eta_0/n$, where $\eta_0 = 377\ \Omega$ (wave impedance of free space) and $n = 2.1$ is the refractive index $[n = (\varepsilon_r)^{\frac{1}{2}}; \varepsilon_r = 4.4]$ of the Z-cut quartz in the microwave-to-THz region. Because the graphene is so much thinner than an RF wavelength, it can be represented by a parallel impedance Z_G at the input port of the

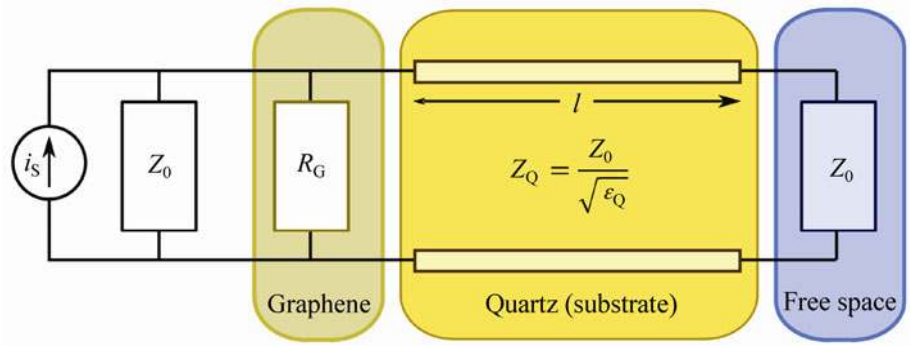

Figure S-6 Alternative for Fig. 3 in the main manuscript

transmission line. The radiation propagating on the transmitted side will be unidirectional (guided-wave or TEM mode), so its behavior can be added simply as a load impedance $Z_0 = \eta$ —the wave-impedance of the guided or TEM mode—at the end of the quartz transmission line. The loaded-transmission-line impedance is given by the standard expression [13]

$$Z(l) = Z_Q \frac{Z_0 + jZ_Q \tan(kl)}{Z_Q + jZ_0 \tan(kl)}$$

where $k = \frac{\omega}{v}$ and $v = \frac{c}{n}$, the wave velocity in quartz. Any absorptive losses in the quartz have been ignored (a good assumption for the present quartz substrates up to at least 1.0 THz). The power transmissivity is then the ratio of the power delivered to the "load", P_L, divided by the power available from the source, P_A:

$$T \equiv \frac{P_L}{P_A} = \frac{\left(\frac{1}{2}\right) i_S^2 \left| \frac{Z_0 \parallel Z_G}{Z_0 \parallel Z_G + Z(l)} \right|^2 \mathrm{Re}[Z(l)]}{\left(\frac{1}{8}\right) i_s^2 Z_0}$$

This expression is expected to be <1 because of power dissipated in the graphene and power reflected back to the source by the frequency-dependent standing-wave interference in the quartz substrate. It also accounts for the possible reactive impedance (imaginary part of Z_G) in the graphene film.

THz calibrations

The measured THz transmission amplitude was fitted to Eq. (3), and values of n = 1.93 and L = 562 μm were found as the best fit to the standing wave pattern. Once the values of n and L were obtained, the sheet conductivity could be determined. Shown in Fig. S-7 below is a prediction of Eq. (5) for various values of a simple toy model of a frequency-independent sheet conductivity (plotted for values between 0.001 mS to 1 mS), and also shown is the SLG and MLG transmission data. It is clear that the data for the MLG allow the effective determination of the sheet conductance, which is ~1 mS. However, for the SLG data, the measurement noise does not allow determination of sigma if it is less that 0.1 mS (i.e. we cannot distinguish between the blue, pink, yellow curves and the SLG data), which seems to be the case for the SLG data. For the MLG data, instead of assuming a frequency-dependent conductance (which is modeled in Fig. S-7 below), we determined the actual measured conductance at each frequency, by solving Eq. (5) for σ.

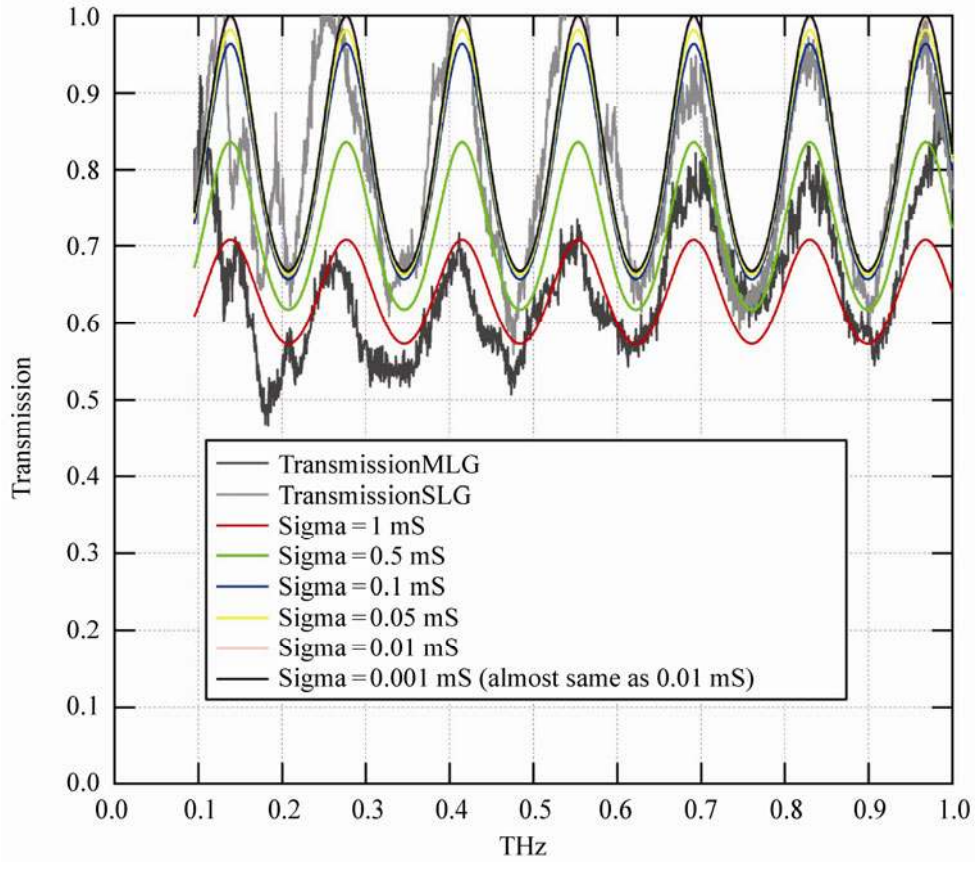

Figure S-7 Predicted transmission (with Fabry–Pérot effect modeled in) for various values of sheet conductance, and the measured MLG and SLG data

Detailed table for all samples

Serial #	Sample #	Raman, # of layer(s)	DC, R_s (kΩ/sq.)	10 GHz, R_s (kΩ/sq.)	100 GHz, R_s (kΩ/sq.)	1 THz, R_s (kΩ/sq.)
MLG						
Sample 1 (damaged)	1		1.7	1.17		
Sample 2 (damaged)	2					
Sample 3	3		~4	2.53		
Sample 4	4			1.28		0.5
Sample 5	5	4		1.54		
Sample 6	6			1.57		
Sample 7	7	5–6		1.5	0.7	
Sample 8	8			1.11		
Sample 9	9	3		1.14	0.705	
Sample 10	10			1.04		
Sample 11	11	2–3		1.16	0.78	
Sample 12	12			1.4	0.8	
SLG						
Sample 1	SLG 1	1		~7.8	~6.3	X
Sample 2	SLG 2	1		~6.5	~6.6	X

References

[1] Reina, A.; Jia, X.; Ho, J.; Nezich, D.; Son, H.; Bulovic, V.; Dresselhaus, M. S.; Kong, J. Large area, few-layer graphene films on arbitrary substrates by chemical vapor deposition. *Nano Lett.* **2009**, *9*, 30–35.

[2] Li, X.; Cai, W.; An, J.; Kim, S.; Nah, J.; Yang, D.; Piner, R.; Velamakanni, A.; Jung, I.; Tutuc, E., et al. Large-area synthesis of high-quality and uniform graphene films on copper foils. *Science* **2009**, *324*, 1312–1314.

[3] Yan, Z.; Peng, Z. W.; Sun, Z. Z.; Yao, J.; Zhu, Y.; Liu, Z.; Ajayan, P. M.; Tour, J. M. Growth of bilayer graphene on insulating substrates. *ACS Nano* **2011**, *5*, 8187–8192.

[4] Peng, Z. W.; Yan, Z.; Sun, Z. Z.; Tour, J. M. Direct growth of bilayer graphene on SiO_2 substrates by carbon diffusion through nickel. *ACS Nano* **2011**, *5*, 8241–8247.

[5] Ferrari, A. C.; Meyer, J. C.; Scardaci, V.; Casiraghi, C.; Lazzeri, M.; Mauri, F.; Piscanec, S.; Jiang, D.; Novoselov, K. S.; Roth, S., et al. Raman spectrum of graphene and graphene layers. *Phys. Rev. Lett.* **2006**, *97*, 187401.

[6] Graf, D.; Molitor, F.; Ensslin, K.; Stampfer, C.; Jungen, A.; Hierold, C.; Wirtz, L. Spatially resolved Raman spectroscopy of single- and few-layer graphene. *Nano Lett.* **2007**, *7*, 238–242.

[7] Malard, L. M.; Nilsson, J.; Mafra, D. L.; Elias, D. C.; Brant, J. C.; Plentz, F.; Alves, E. S.; Neto, A. H. C.; Pimenta, M. A. Electronic properties of bilayer graphene probed by resonance Raman scattering. *Phys. Status Solidi B* **2008**, *245*, 2060–2063.

[8] Casiraghi, C. Doping dependence of the Raman peaks intensity of graphene close to the Dirac point. *Phys. Rev. B* **2009**, *80*, 233407.

[9] Zhang, B.; Lee, W. H.; Piner, R.; Kholmanov, I.; Wu, Y. P.; Li, H. F.; Ji, H. X.; Ruoff, R. S. Low-temperature chemical vapor deposition growth of graphene from toluene on electropolished copper foils. *ACS Nano* **2012**, *6*, 2471–2476.

[10] Lenski, D. R.; Fuhrer, M. S. Raman and optical characterization of multilayer turbostratic graphene grown via chemical vapor deposition. *J. Appl. Phys.* **2011**, *110*, 013720.

[11] Kim, H.; Mattevi, C.; Calvo, M. R.; Oberg, J. C.; Artiglia, L.; Agnoli, S.; Hirjibehedin, C. F.; Chhowalla, M.; Saiz, E. Activation energy paths for graphene nucleation and growth on Cu. *ACS Nano* **2012**, *6*, 3614–3623.

[12] Yan, J.; Zhang, Y.; Kim, P.; Pinczuk, A. Electric field effect tuning of electron-phonon coupling in graphene. *Phys. Rev. Lett.* **2007**, *98*, 166802.

[13] Ulaby, F. T. *Fundamentals of Applied Electromagnetics*; Pearson: Upper Saddle River, NJ, 2004.